AGU PUBLICATIONS

Journal of Advances in Modeling Earth Systems

RESEARCH ARTICLE
10.1002/2016MS000892

Improvements to the snow melting process in a partially double moment microphysics parameterization

Bonnie R. Brown[1,2], Michael M. Bell[1,3], and Gregory Thompson[4]

[1]Department of Atmospheric Sciences, University of Hawai'i, Manoa, Honolulu, Hawai'i, USA, [2]Now at National Disaster Preparedness Training Center at the University of Hawai'i, NOAA Inouye Regional Center, Honolulu, Hawai'i, USA, [3]Department of Atmospheric Science, Colorado State University, Fort Collins, Colorado, USA, [4]Research Applications Laboratory, National Center for Atmospheric Research, Boulder, Colorado, USA

Key Points:
- Median rain drop size is too large in stratiform rain using the original Thompson-Eidhammer scheme
- Rain number production by snow melting is identified as process for producing large median drop size
- Modifications to the snow melting process lead to improved comparison with radar observations

Correspondence to:
M. M. Bell,
mmbell@colostate.edu

Citation:
Brown, B. R., M. M. Bell, and G. Thompson (2017), Improvements to the snow melting process in a partially double moment microphysics parameterization, *J. Adv. Model. Earth Syst.*, *9*, 1150–1166, doi:10.1002/2016MS000892.

Received 12 DEC 2016
Accepted 19 APR 2017
Accepted article online 25 APR 2017
Published online 14 MAY 2017

Abstract Polarimetric upgrades to the U.S. radar network have allowed new insight into the precipitation processes of tropical cyclones. Previous work by the authors compared the reflectivity at horizontal polarization and differential reflectivity observations from two hurricanes to simulated radar observations from the WRF model, and found that the aerosol-aware Thompson-Eidhammer microphysical scheme performed the best of several commonly used bulk microphysical parameterizations. Here we expand our investigation of the Thompson-Eidhammer scheme, and find that though it provided the most accurate forecast in terms of wind speed and simulated radar signatures, the scheme produces areas in which the differential reflectivity was much higher than observed. We conclude that the Thompson-Eidhammer scheme produces drop size distributions that have a larger median drop size than observed in regions of light stratiform precipitation. Examination of the vertical structure of simulated differential reflectivity indicates that the source of the discrepancy between the model and radar observations likely originates within the melting layer. The treatment of number production of rain drops from melting snow in the microphysical scheme is shown to be the ultimate source of the enhancement of differential reflectivity. A modification to the scheme is shown to result in better fidelity of the radar variables with the observations without degrading the short-term intensity forecast. Additional tests with an idealized squall line simulation are consistent with the hurricane results, suggesting the modification is generally applicable. The modifications to the Thompson-Eidhammer scheme shown here have been incorporated into updates of the WRF model starting with version 3.8.1.

1. Introduction

Recent dual-polarization upgrades to the United States' Next-Generation Radar (NEXRAD) network of WSR-88D S-band radars have brought widespread polarimetric coverage to the continental United States, Hawaii, Alaska, and Puerto Rico. The upgrade has allowed new types of measurements to be made which improve the estimation of precipitation size, amount, and type. As tropical cyclones (TCs) have passed close to newly upgraded coastal radar locations, unprecedented measurements of their precipitation structure are now available. This will allow much needed investigation into the microphysical processes occurring in TCs and their representation in numerical model simulations.

Although both operational track and intensity forecasts of TCs have exhibited improvement over the past decades, improvements in track prediction have far outpaced the improvement in intensity prediction [e.g., *DeMaria et al.*, 2014; *Emanuel and Zhang*, 2016]. The discrepancy in skill has been attributed to a lack of understanding and accurate representation of the multiscale interactions within and around TCs which strongly affect the intensity. Uncertainty in the microphysics of TCs make up a significant component of the intensity prediction challenge, both because of the large release of latent heat from microphysical processes that interact nonlinearly with the dynamics of the storm and the limits of microphysical observations in TCs. Ground-based and aircraft-based in situ microphysical measurements represent only point observations, while polarimetric radar measurements, which offer wider coverage, require a storm to pass within the radar range. Since the polarization upgrade of the NEXRAD network, two hurricanes that tracked closely to coastal radars were Arthur (2014), which affected North Carolina, and Ana (2014) which passed south of the Hawaiian Islands, both of which we study here.

© 2017. The Authors.
This is an open access article under the terms of the Creative Commons Attribution-NonCommercial-NoDerivs License, which permits use and distribution in any medium, provided the original work is properly cited, the use is non-commercial and no modifications or adaptations are made.

Polarimetric radar observations have begun to reveal new insight into the precipitation processes of TCs. The addition of a vertically polarized beam to the traditional, horizontally polarized beam allows for comparison of the returned power from each via the difference (differential reflectivity Z_{DR}), correlation (copolar correlation coefficient ρ_{hv}), and difference in phase shift (differential propagation shift Φ_{DP} and specific differential phase shift K_{DP}), detailed descriptions of which can be found in *Kumjian* [2013]. Here we use the differential reflectivity (Z_{DR}), which can also be calculated as the logarithmic ratio of the returned power of the horizontally to vertically polarized backscatter, and uses units of decibels (dB). Hydrometeors with a horizontal axis that is larger than their vertical axis will return a positive Z_{DR}; due to liquid drops' tendency to increase oblateness as they grow, Z_{DR} tends to be positive in areas of rain and tends to increase with increasing raindrop size. While the radar reflectivity factor at horizontal polarization (Z_H) is dependent on hydrometeor number concentration, Z_{DR} is independent of it; thus, using Z_H and Z_{DR} together provides new information on the drop size distribution (DSD) of the observed precipitation [*Brandes et al*., 2004a; *Kumjian*, 2013]. Polarimetric radar observations have recently been made of landfalling TCs in Australia [*May et al*., 2008], the United States [*Kosiba et al*., 2013; *Kosiba and Wurman*, 2014], and China [*Wang et al*., 2016] using research and/or mobile radars. Utilizing a permanent, operational polarized radar network such as NEXRAD will facilitate more generalized, long-term studies of both the microphysical characteristics of TCs themselves and the numerical representation thereof, providing a crucial expansion on the above-cited case studies.

Current numerical predictions of TCs, as with other weather phenomena, have the option of using more complex microphysical parameterizations with more degrees of freedom than in the past, thanks to increasing computational capabilities. After comparing the sensitivity of the rainfall using single-moment and double-moment microphysical schemes to changes in the fixed parameters, *Igel et al*. [2015] recommended that all numerical weather prediction studies utilize a double-moment scheme because they were found to be more accurate and less sensitive to arbitrary changes to the fixed parameters. Indeed, *Jin et al*. [2014] found that choosing a double-moment scheme (the Thompson scheme modified for use in the TC version of the Coupled Ocean and Atmosphere Mesoscale Prediction System (COAMPS-TC) [*Doyle et al*., 2014]) produced better TC intensity predictions than COAMPS baseline predictions using a single-moment microphysical scheme. *Jin et al*. [2014] attributed the improvements in COAMPS-TC predictions specifically to the double-moment treatment of ice-phase microphysics and the conversion of ice crystals to snow flakes. However, due to the nonlinear interactions of the microphysics parameterization with other components of the modeling system, TC simulations remain highly sensitive to the choice of microphysics scheme, regardless of the degrees of freedom used, as highlighted by works such as *Brown et al*. [2016] (hereafter BBF16), *Fovell et al*. [2009, 2016], *Penny et al*. [2016], *Khain et al*. [2015], and *Pattnaik et al*. [2011].

In this study, we investigate further the source of discrepancies in radar variables between TC simulations using the aerosol-aware *Thompson and Eidhammer* [2014] microphysical parameterization in the Weather Research and Forecasting (WRF) model, and polarimetric radar observations that were originally identified in BBF16. The remainder of the paper is organized as follows: Section 2 describes the polarimetric radar observations from the NEXRAD network that are used to validate the simulations, as well as the model setup and pertinent details of the microphysical scheme. Section 3.1 shows the distribution of the simulated radar variables from the original configuration of the Thompson-Eidhammer scheme and compares them to the radar observations, and the results of modifying the parameterization are presented in section 3.2. Tests with an idealized midlatitude squall line are presented in section 3.3 to confirm the generality of the results. Finally, the implications of the results and concluding remarks are given in section 4.

2. Data and Methods

2.1. Radar Measurements

Hurricane Arthur was the first named storm of the 2014 North Atlantic hurricane season and achieved hurricane strength early on 3 July of that year. Arthur had a peak intensity of 43.7 m s^{-1} (85 kts) at 0000 UTC 4 July and made landfall several hours later near Cape Lookout, NC [*Berg*, 2015]. Arthur was within observable range of the NEXRAD radars at Wilmington (KLTX) and Morehead City (KMHX), NC, during its period of peak intensity. Hurricane Ana was the first named storm to originate in the Central Pacific in 2014, and achieved hurricane strength early on 17 October. Ana had a peak intensity of 38.6 m s^{-1} (75 kts) at 0600 UTC 18

October [*Powell*, 2014] and the center passed just south of the Hawaiian Islands. Ana was observed by the radars at Lihue, Kauai (PHKI), and Molokai (PHMO), HI after peak intensity.

Three hours of Level II data for each storm were obtained from NOAA's National Climatic Data Center for each of the radar sites mentioned above corresponding with the last 3 h of WRF simulation for each storm. The data were then gridded to the model resolution and composited by selecting the radar reflectivity factor at horizontal polarization (Z_H) and differential reflectivity (Z_{DR}) from the radar site with the highest Z_H for each point, implying a less attenuated signal or closer range to the radar. Basic quality control to remove nonmeteorological and unphysical radar echoes was performed as described in supporting information S3 of BBF16. Typical calibration for differential reflectivity measurements is usually accomplished by vertically pointing the beam of the radar; however, NEXRAD radars are incapable of observing directly overhead, so an alternative method of Z_{DR} calibration was performed using the light rain/low elevation angle method of *Cunningham et al*. [2013]. The biases were found and corrected for 0 dB for PHKI, −0.1 dB for PHMO, +0.15 for KLTX, and +0.15 dB for KMHX.

2.2. Numerical Model Configuration

To achieve the goal of evaluating the representation of microphysical processes in simulated TCs, the radar measurements were compared to various simulations of hurricanes Arthur and Ana in the WRF-ARW model, version 3.6.1, as in BBF16. The model domain consists of four, two-way nested domains at 18, 6, 2, and 2/3 km resolution on 300, 250, 250, and 400 grid points square, respectively. The inner domains are vortex-following using the pressure minimum at 700 hPa. All domains in all simulations used the following physics parameterizations: RRTM long wave radiation [*Mlawer et al*., 1997], Dudhia shortwave radiation [*Dudhia*, 1989], the Noah land-surface model [*Ek*, 2003], the Yonsei University boundary layer scheme [*Hong et al*., 2006], and modified surface fluxes for tropical cyclones with a one-dimensional ocean mixed layer model [*Davis et al*., 2010]. The outer two domains used the Kain-Fritsch cumulus parameterization [*Kain and Fritsch*, 1990] while there are no cumulus parameterizations on the inner two domains.

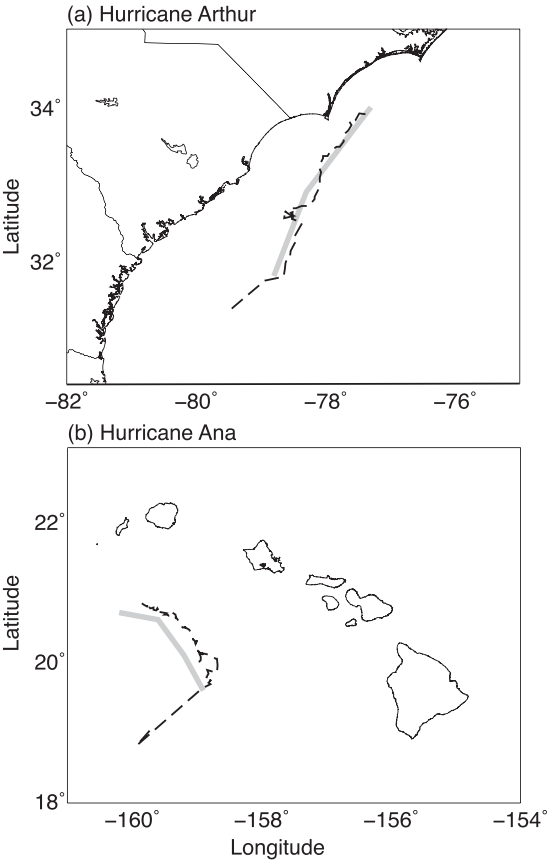

Figure 1. Tracks of Hurricane (a) Arthur and (b) Ana during the simulation period. Thin dashed line indicates simulated tracks from WRF, and thick gray line indicates observed best track.

The model was initialized with the GFS (FNL) analysis at 1.0° resolution. The Arthur case was initialized at 1200 UTC on 3 July 2014 and run for 12 h. The Ana case was initialized at 0000 UTC on 19 October 2014 and run for 18 h. The simulated tracks of Arthur and Ana and nearby coastlines are shown in Figure 1. The initial positions are displaced from the surface-based best track due to the broad 700 hPa vortex from the relatively coarse initial conditions, but are generally in good agreement with the observed track after a short spin-up period. The results presented in this study are calculated using the 2/3 km domain at 15 min output unless otherwise specified. We note that the temporal resolution of the model output is lower than that of the radar data, but produces enough output for an adequate statistical comparison with the radar observations. The results were not sensitive to the specific length of time used to calculate the statistics as long as there were a sufficient number of points to accurately describe the probability distribution.

2.3. Microphysical Parameterization

The same microphysics scheme was used for all four domains in each simulation. *Brown et al*.

[2016] tested several single-moment and double-moment microphysical schemes using this model configuration and found that the most accurate bulk microphysical parameterization, in terms of both 10 m peak wind speed and simulated radar variables, was the aerosol-aware Thompson-Eidhammer scheme (referred to as Thompson-Eidhammer hereafter, described by *Thompson et al*. [2008] and *Thompson and Eidhammer* [2014], hereafter TE14), which is partially double-moment. We chose the Thompson-Eidhammer scheme to conduct further experiments with in this study, and it is described in detail below. The output of the microphysical scheme is used to simulate the radar reflectivity factor and differential reflectivity using the method of *Jung et al*. [2010] as described in BBF16 and supporting information S2 thereof.

The Thompson-Eidhammer microphysical parameterization as implemented in WRF-ARW V3.6.1 is partially double-moment; that is, it predicts both the number concentration and mixing ratio for cloud water droplets, rain drops, and pristine ice particles, and only the mixing ratio for snow and graupel. It also predicts number concentration for cloud condensation nuclei (CCN) and ice nucleating (IN) aerosols, the mass of which is not predicted. A full description of the microphysical scheme can be found in the sources above; here we specifically detail the snow melting process, which is relevant to this study. The number production of rain drops from melting snow is handled thusly:

$$\left[\frac{dn_r}{dt}\right]_{sml} = \frac{\mathcal{M}_0 10^{mT_c}}{q_s \rho}\left[\frac{dq_r}{dt}\right]_{sml} \tag{1}$$

where *sml* indicates process rates due to melting of snow, n_r, q_r, and q_s are the number concentration and mixing ratio of rain, and the mixing ratio of snow, T_c is the temperature in centigrade, ρ is the moist air density, and $\mathcal{M}_0$ is the zeroth moment of the snow particle distribution (PSD), i.e.,

$$\mathcal{M}_0 = \int N(D) dD, \tag{2}$$

representing the number concentration, which can be readily diagnosed at all grid points in the model using the scheme's internal assumptions. The constant m in equation (1) is a tunable parameter; if snow were represented in a double-moment fashion, m would essentially be zero and $\mathcal{M}_0$ would be a predicted number concentration. Because snow number concentration is not predicted, the value 10^{mT_c} is an artificial means of reducing $\mathcal{M}_0$ during the melting process. In V3.6.1 of the WRF model, m is set equal to -0.75 in the Thompson-Eidhammer scheme, and the model simulations of Ana and Arthur first introduced in BBF16 using this configuration are termed the M75 experiment. Though somewhat arbitrary, the control value for m of -0.75 was originally chosen to maintain a constant vertical profile of radar reflectivity below the melting layer. Also, an additional constraint was imposed in this version of the code whereby rain number production from melting snow is omitted entirely if the snow mixing ratio is less than 0.005 g kg^{-1} or the air temperature is greater than 3.5°C. Rain number production from melting graupel is given a similar treatment to snow melting processes; however, we find that graupel melting processes have little effect in the hurricane environments studied here due to very low amounts of graupel.

Many processes modeled by a microphysics scheme could contribute to the over-large median drop size noted in BBF16, including the processes of drop breakup and self-collection. In the Thompson-Eidhammer scheme, these processes are modeled in a similar manner to that described in *Morrison et al*. [2012] using a bulk collection efficiency for rain self-collection Ef_{rr}. This parameter is positive for DSDs with a median volume diameter below a critical threshold $D0_{th}$ resulting in a decrease in the raindrop number concentration due to self-collection. Above the threshold, Ef_{rr} becomes negative and results in an increase in the number concentration due to the drop breakup. The amplitude of the number concentration tendency can be further adjusted through a weighting function denoted here as α_{nr}, which is multiplied times the efficiency, current number concentration, and liquid water content. The control values of these parameters in V3.6.1 are 1.95 mm for $D0_{th}$ and 0.5 for α_{nr}, and were chosen based on the results of *Nissan and Toumi* [2013] that identified signals of both over-active drop breakup and self-collection in the previous versions of the Thompson-Eidhammer scheme. In this study, we primarily focus on the snow melting process, but examine the effects of modifying these parameters in section 3.3.

3. Results

3.1. Simulated Drop Size Distributions

BBF16 introduced a joint probability distribution function (JPDF) diagram which shows the frequency of occurrence of pairs of Z_H and Z_{DR} within a spatial volume and during a set time interval. These JPDFs are normalized by the peak frequency, such that 100% represents the most commonly occurring joint value of horizontally polarized reflectivity and differential reflectivity, and the values over 50% are referred to as the modal distribution following *Hence and Houze* [2011]. The JPDFs of the radar observations, as calculated in BBF16, show that the modal distribution is contained within 20–40 dBZ in Z_H and 0–1 dB in Z_{DR} in hurricane Arthur (Figure 2a). The modal distribution of hurricane Ana (Figure 2b) is similarly contained within 30–40 dBZ and 0–1.25 dB. The distribution of values 5% of the peak frequency or greater is observed not to exceed 45 dBZ and 1.5 dB for both hurricanes. Negative values of differential reflectivity observed by the radar are likely unphysical noise.

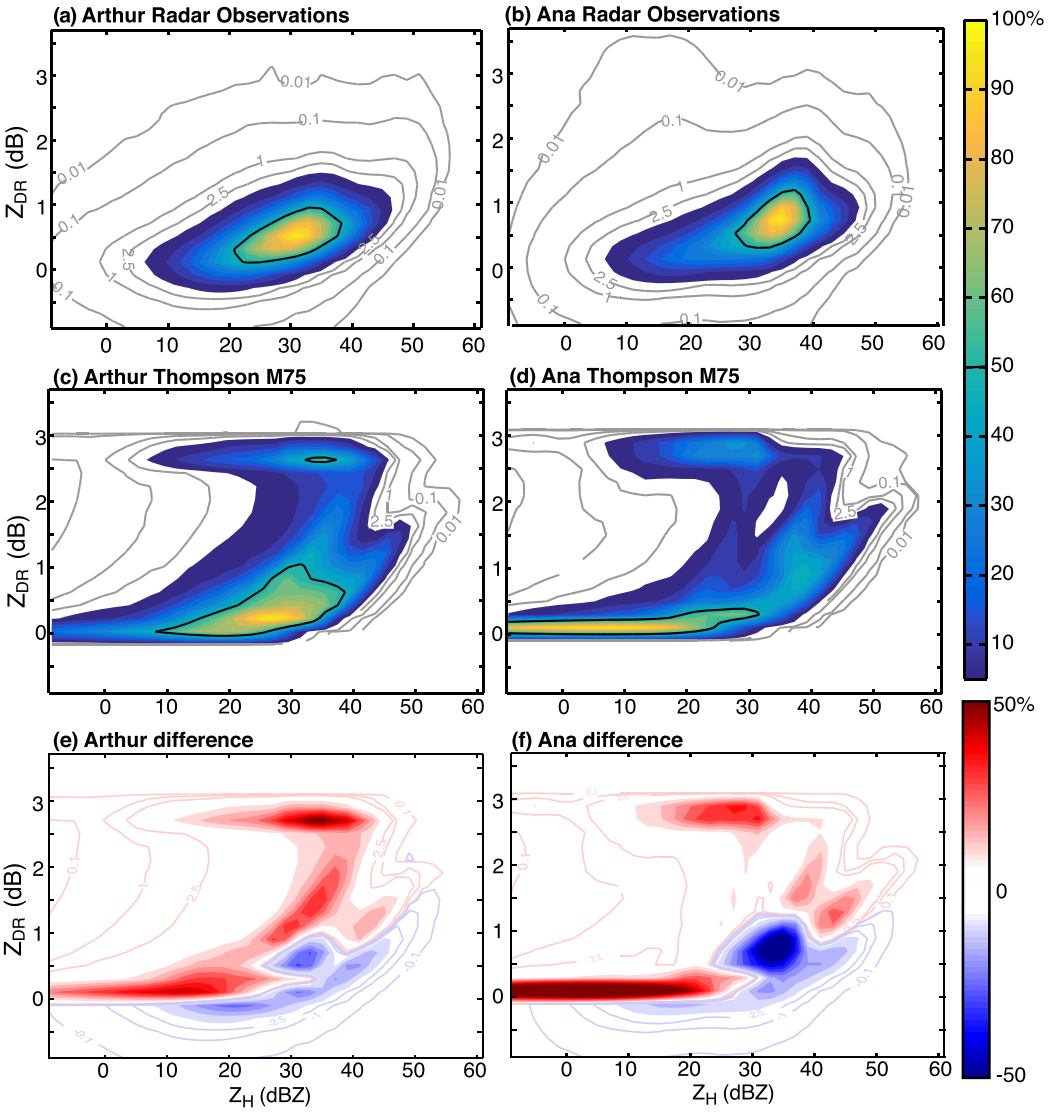

Figure 2. The joint frequency of radar reflectivity factor at horizontal polarization (abscissa) and differential reflectivity (ordinate) over 3 h normalized by the maximum frequency in each data set, with 50% contoured in black and 0.01%, 0.1%, 1%, and 2.5% contoured in gray. Distributions for the radar measurements of (a) Arthur and (b) Ana use observations below 3.25 km. Distributions from WRF simulation M75 innermost domain (c, d) are restricted to below 3.3 km. The difference of the middle row from the top row is shown in Figures 2e and 2f, with 0.1%, 1%, and 2.5% contoured in light red and −0.1%, −1%, and −2.5% contoured in light blue. Figures 2a–2d are reproduced from *Brown et al.* [2016, Figure 3].

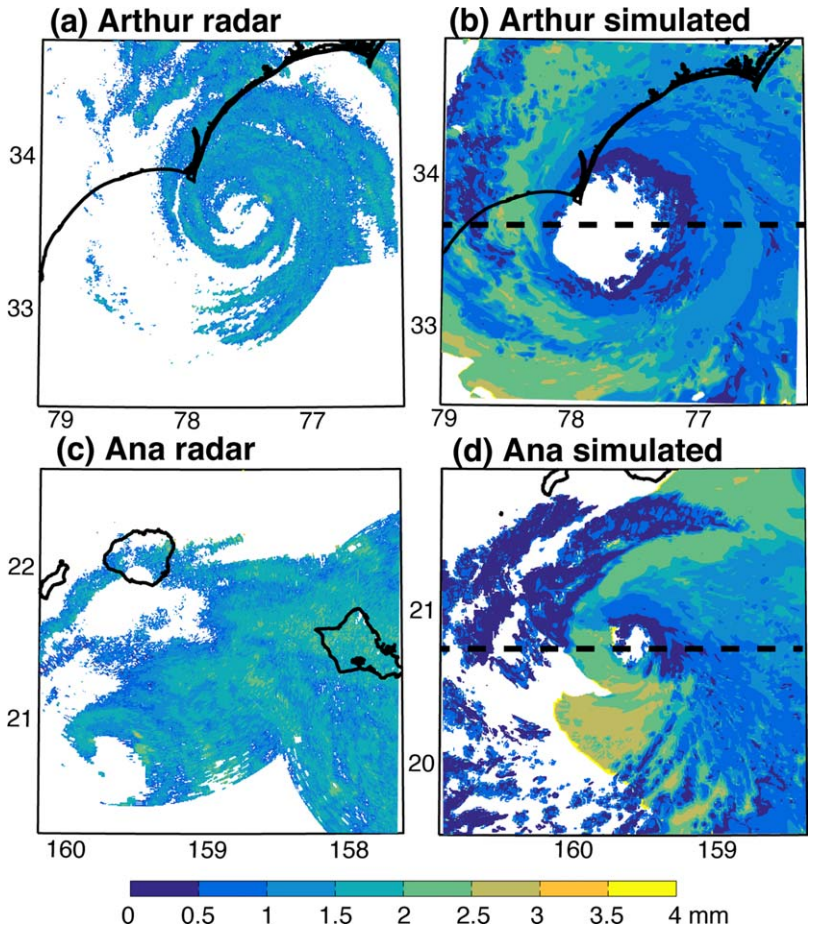

Figure 3. Median drop size (D_0) for (a, c) Arthur and Ana as measured by the radar (calculated from Z_{DR} via *Brandes et al.* [2004b]; only points with $Z_{DR} \geq 0$ shown) and (b, d) simulated by the unmodified (M75) Thompson-Eidhammer scheme (calculated from the slope parameter of the gamma distribution via *Ulbrich* [1983]) at 2230 on 3 July 2014 and 1630 UTC on 19 October 2014, respectively. All data are shown at an altitude of 2 km. Dashed lines in Figures 3b and 3d indicate location of vertical cross sections shown in Figure 4.

While the simulated distributions exhibit similarities to the radar observations, generally showing the same positive relationship between Z_H and Z_{DR} with modal and extreme values of reflectivity limited to below 40 and 55 dBZ, respectively (Figures 2c and 2d), BBF16 did find notable differences between the simulated and observed radar variables. The plots of the difference between the radar observed and simulated JPDFs are calculated as in, for example, Figure 3 of *DeHart et al*. [2014] and shown in Figures 2e and 2f. The difference JPDFs reveal a region between 2 and 3 dB in Z_{DR} at moderate Z_H values that is present at frequencies up to 50% in the simulation but not the observations. Other regions of discrepancy include areas of Z_H below 10 dBZ, where the S-band radar has low or no sensitivity at longer range [e.g., *White et al*., 2000], and areas of Z_{DR} below 0 dB, which are likely due to unphysical noise in the radar measurements. It is also clear from Figure 2f that the simulated modal distribution for Ana occurs at lower Z_H values than the observed, but because this area of difference is contained by the 5% frequency contour and not reproduced in Arthur, we choose to focus on the region at larger Z_{DR} noted above, which is consistent between both storms.

A horizontal cross section of the median drop size (D_0) at a constant altitude of 2 km is shown in Figure 3. As noted above, a relatively larger Z_{DR} indicates a relatively larger D_0 in a liquid drop population, and the two values are proportional when using a gamma distribution to describe the DSD [*Brandes et al*., 2004b; *Ulbrich*, 1983]. Areas of larger median drop sizes (larger than 2 mm) relative to the radar measurements are apparent in the simulated stratiform regions of the storm, coincident with low to moderate values of Z_H (Figures 3b and 3d; see BBF16 Figures 1 and 2 for reflectivities). Using the relationship of Z_{DR} and median drop size described in *Brandes et al*. [2004b], the median drop size as measured by the NEXRAD radar

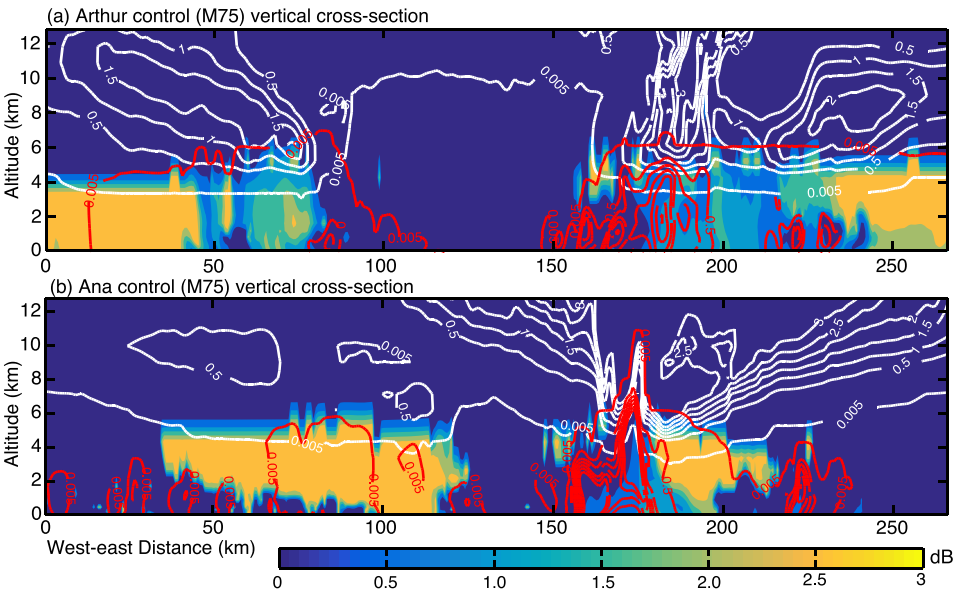

Figure 4. A vertical cross section of the WRF simulations in the east-west direction that traverses the eye of (a) Arthur at 2230 UTC on 3 July 2014 and (b) Ana at 1630 UTC on 19 October 2014 south of the center showing differential reflectivity (shading, dB), rain mixing ratio (red contours, g kg^{-1}) and snow mixing ratio (white contours, g kg^{-1}).

composites clearly show less area encompassed by 2 mm or larger D_0 at the same time and altitude as compared to the WRF simulations (Figures 3a and 3c). On the basis of these validating radar observation sets, we conclude that the Thompson-Eidhammer scheme produces DSDs with a median drop size that is larger than observed.

To investigate further the source of the discrepancy between the observed and the simulated DSD, vertical cross sections are taken through the simulated TCs shown in Figure 4. These cross sections are taken in the west to east direction, transecting the eye of Arthur and Ana south of the center of circulation such that areas of high Z_{DR} and moderate Z_H are captured. Since simulated Z_{DR} is only calculated for liquid drops, we do not expect to observe a bright band or any differential reflectivity above the melting layer in the WRF simulations. The cross sections show that the regions of high Z_{DR} and large median drop size extend through a deep layer from the surface to the melting layer. Furthermore, these vertically deep areas of large Z_{DR} tend to occur in areas of low rain mixing ratio, and below regions of low snow mixing ratio, which is consistent with the observation that they tend to occur in stratiform areas of low to moderate Z_H. In contrast, regions of convective activity with discrete shafts of large rain and snow mixing ratio exhibit values of Z_{DR} that vary in the vertical and have a value closer to those observed by radar (e.g., at 175 km in Figures 4a and 4b).

3.2. Results of Parameterization Modification

It appears that, in the case of the Thompson-Eidhammer scheme, erroneously large Z_{DR} values may originate with DSDs that form in the melting layer. Thus, it is reasonable to investigate the effect of melting frozen hydrometeors on the rain DSD. As discussed in section 2.2, the rain number production from melting snow is a prime candidate for experimentation because the calculation contains an arbitrary and tunable parameter referred to as *m* here. The purpose of the term containing *m* in the exponent is to artificially reduce the number of particles melting into rain, thus *m* must be negative to ensure the term is less than one. Two experiments were conducted to make *m* less negative to −0.20 (increase number of rain drops from melted snow) and more negative to −1.75 (decrease rain drops from melted snow; M20 and M175, respectively, see Table 1). Additionally, two experiments were conducted removing the portion of the parameterization that omits rain number production from snow melting if the snow mixing ratio is less than 0.005 g kg^{-1} or the air temperature is greater than 3.5°C. The *m* value was tested at the original value of −0.75 (M75noif) and at the value of −0.20 (M20noif) for these two experiments. Experiments M75noif and M20noif are conducted because areas of enhanced Z_{DR} appear to occur preferentially below regions of

Table 1. Description of Microphysical Parameterization Modification Experiments

Name	Description
M75	Snow melt exponential constant m set to −0.75 (original V3.6.1 configuration)
M20	Snow melt exponential constant m set to −0.20
M175	Snow melt exponential constant m set to −1.75
M75noif	Snow melt exponential constant m set to −0.75 and "if" statement omitted
M20noif	Snow melt exponential constant m set to −0.20 and "if" statement omitted
M20Efrr	Snow melting as in M20noif but with $D0_{th}$ = 1.6 mm and α_{nr} = 2.0
M75Efrr	Snow melting as in M75 but with $D0_{th}$ = 1.6 mm and α_{nr} = 2.0

very low snow mixing ratio that may be affected by this logical test, which would reduce the number concentrations of rain drops, increasing the drop size for a given mixing ratio. The original control experiment discussed in the previous section uses the Thompson-Eidhammer scheme as originally configured in WRF V3.6.1 and BBF16 and is termed as M75.

Vertical cross sections of the resulting simulations are presented in Figure 5 for Arthur and Figure 6 for Ana. Decreasing (making more negative) m to −1.75 should have the effect of decreasing the number production of rain

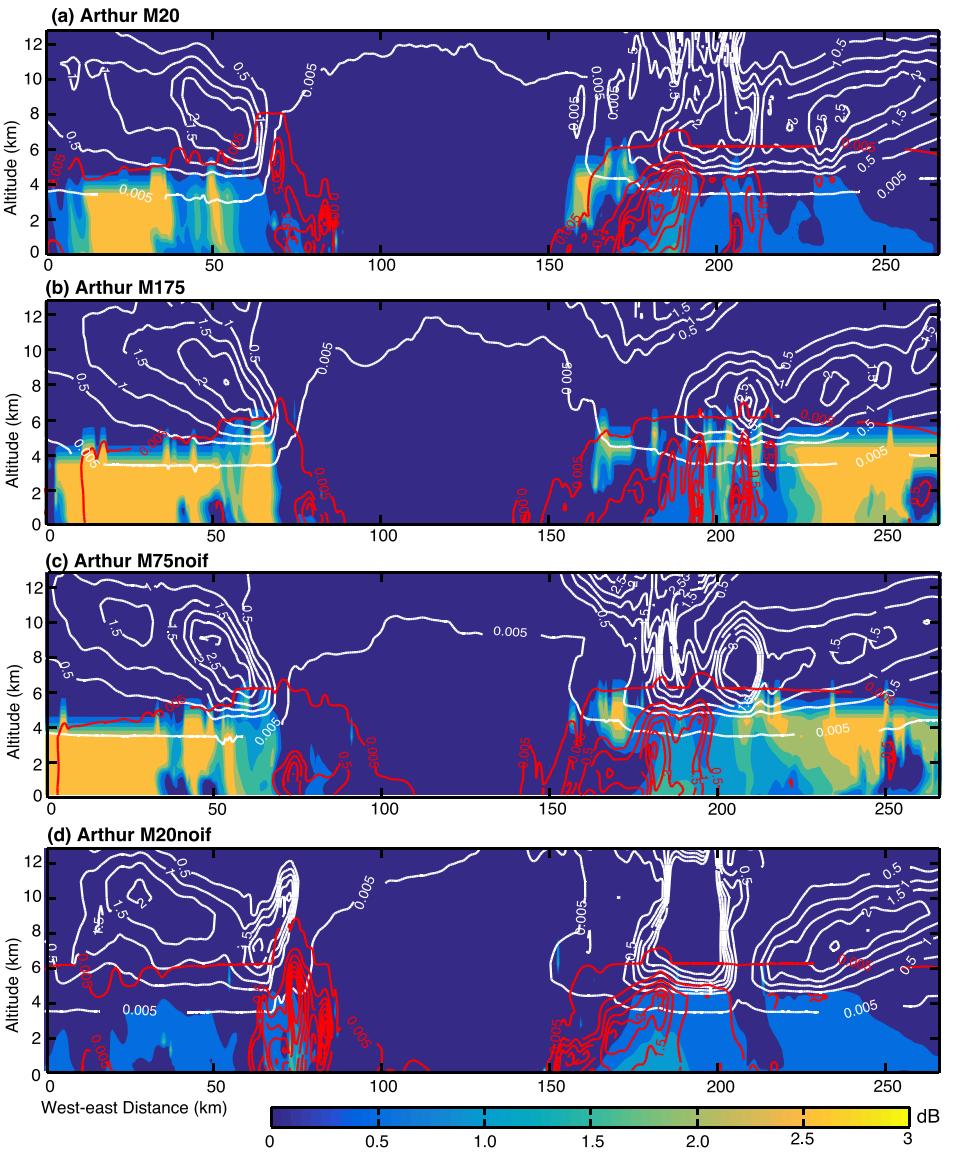

Figure 5. Vertical cross sections of Arthur as in Figure 4a for experiments (b) M20, (c) M175, (c) M75noif, and (d) M20noif.

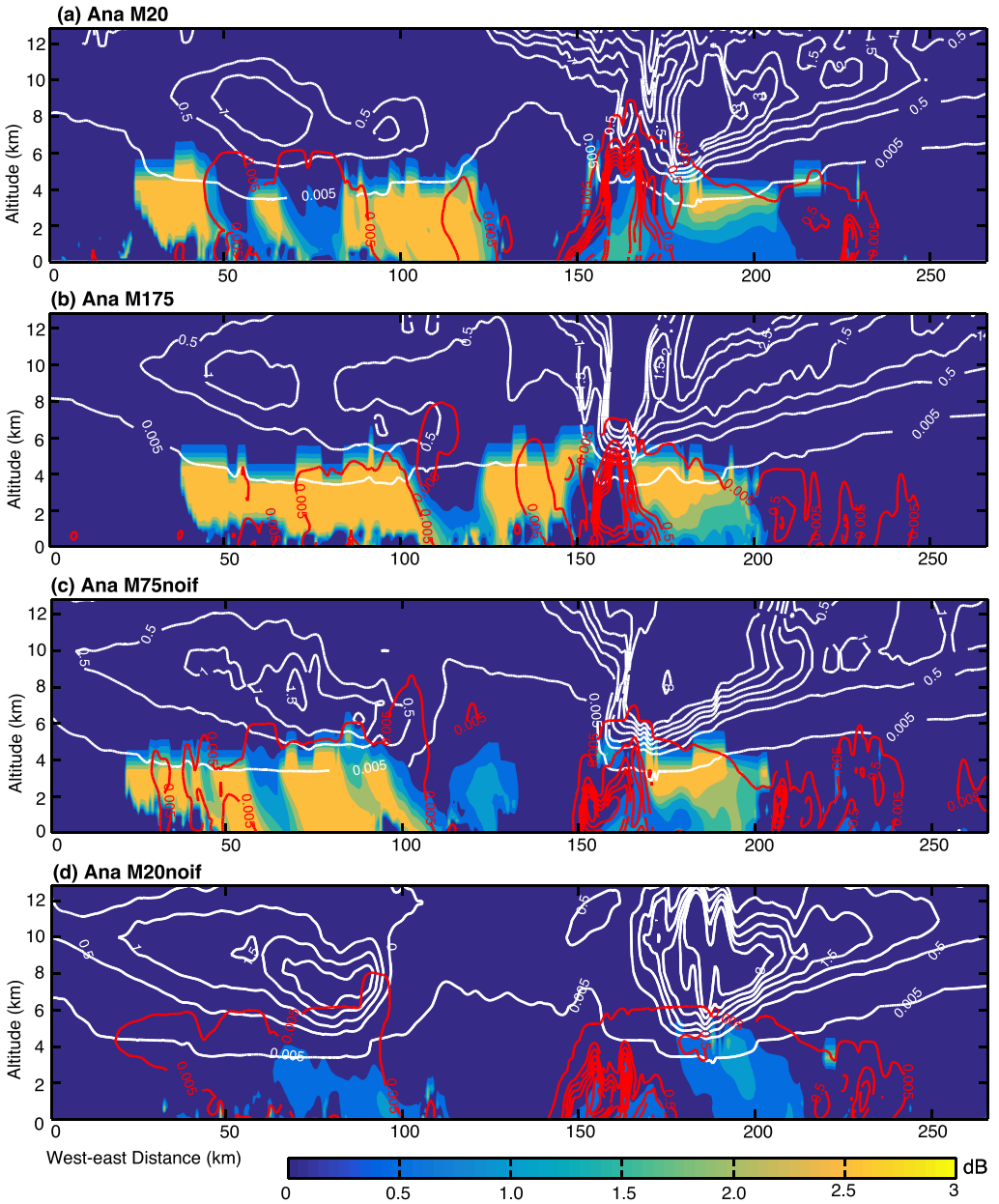

Figure 6. Vertical cross sections of Ana as in Figure 4b for experiments (a) M20, (b) M175, (c) M75noif, and (d) M20noif.

from melting snow, causing there to be fewer drops for a given mixing ratio and increasing the median drop size of the DSD; increasing (making less negative) *m* should have the opposite effect. Indeed, regions of Z_{DR} greater than 2.5 are decreased in M20 (Figures 5a and 6a), and some areas to the east of the eye decrease to around 0.5 dB and exhibit a more variable vertical structure. In contrast, areas of large Z_{DR} in M175 are still abundant and similar to the control simulation (Figures 5b and 6b).

Figures 7a and 7b confirm that the structure of the average vertical Z_{DR} profile of all points in the innermost, 2/3 km resolution domain contains regions of high Z_{DR}. The vertical profile of the average Z_{DR} is relatively uniform below the melting level in the radar observations, in contrast to a distinct positive slope with height in the M75 simulation. The average value of Z_{DR} in the radar observations is smaller than M75 at all vertical levels. Since the average value of Z_{DR} does not describe the tails of the probability distribution, the percentage of points with Z_{DR} values above 2.5 dB at 2 km altitude is shown in Figure 7c. There is a clear correspondence between the percentage of high Z_{DR} values and the melting parameter. It is evident from the vertical

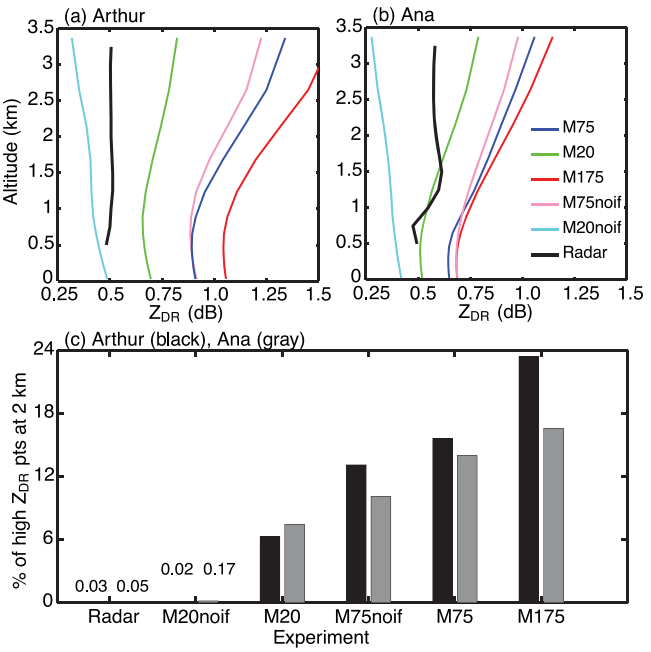

Figure 7. The average vertical profile of Z_{DR} of all points in the 2/3 km domain for the last 3 h of the forecast and the radar composite at the associated times for (a) Arthur and (b) Ana. For the same domain and time period, (c) the percent of points at an altitude of 2 km that have a Z_{DR} greater than or equal to 2.5 dB for Arthur (black) and Ana (gray).

cross sections and statistical analysis that regions of large Z_{DR} have less impact on the overall average vertical profile in M20 than M175 or M75. However, it appears that even in M20, areas of enhanced Z_{DR} in stratiform regions still have a deep and uniform vertical extent beginning at the melting layer, which still influences the slope of the average vertical Z_{DR} with height even though the magnitude is smaller and closer to the radar observations.

Next, the experiments omitting the logical test that shuts off rain number production from snow melting were conducted. When *m* is kept at the original value of −0.75 in experiment M75noif, there appears to be some reduction in the areas of Z_{DR} greater than 2.5 dB in the snapshot cross section (Figures 5c and 6c) and the average vertical profile of Z_{DR} for the full domain exhibits minor improvements similar to those exhibited by M20, namely a less positive slope and a leftward shift (Figures 7a and 7b). M20noif, the experiment which omits the logical statement and increases *m* to −0.20, shows remarkable improvements, reducing the areas of the cross section containing deep layer large Z_{DR} (Figures 5d and 6d). The average profile of Z_{DR} for the full domain is now much closer to that of the radar observations, with a uniform vertical average near about 0.5 dB (Figures 7a and 7b). While additional sources of validation for the vertical profile of Z_{DR} in TCs are scarce, the domain-average result of M20noif is the most consistent of the experiments with the profiles presented in *Wang et al.* [2016, Figure 9j] which showed Z_{DR} generally remaining constant or increasing from the melting layer to the surface. It should be noted, though, that the Z_{DR} profiles of *Wang et al.* [2016] were calculated for convective regions of a typhoon rainband only. Figure 7c clearly shows that as modifications are made to increase the rain number production from melting snow, the percentage of grid points at a reference level of 2 km that exceed or equal 2.5 dB in differential reflectivity is reduced, with experiment M20noif having the lowest percentage of high Z_{DR} points and comparing best to the radar observations. Experiments M20, M75noif, M75, and M175 each have an increasingly larger percentage of high Z_{DR} points, consistent with the decreasing rain number production.

The results of the microphysical parameterization modification experiments are illustrated statistically with difference JPDFs showing the departure of each simulation from the radar observations in Figure 8 for Arthur and Figure 9 for Ana. Compared to the control case, the region of enhanced frequency in the upper portion of the diagram is greatly reduced or eliminated in M20 and M20noif, which have a less negative *m* (Figures 8a, 8c, 9a, and 9c). Alternately, experiments M175, with a more negative *m*, and M75noif, with no change to *m*, do not significantly reduce the noted area of increased frequency. Compared to M75, the region of increased frequency at large differential reflectivity values is actually enhanced in M175, which is consistent with the snapshots shown in Figures 5c and 6c.

It is clear that the maximum benefit is obtained from both modifying *m* to be less negative, thus increasing the raindrop number production from melting snow, and allowing raindrop number production from melting snow in regions with very small snow mixing ratio, where there previously was none. Though the targeted region at large Z_{DR} is suppressed in M20noif, the difference JPDF does not show remedies for other regions of discrepancy with negative Z_{DR} and at very low reflectivity. This is not necessarily due to additional deficiencies in the Thompson-Eidhammer scheme, since, as noted previously, it is likely that observed

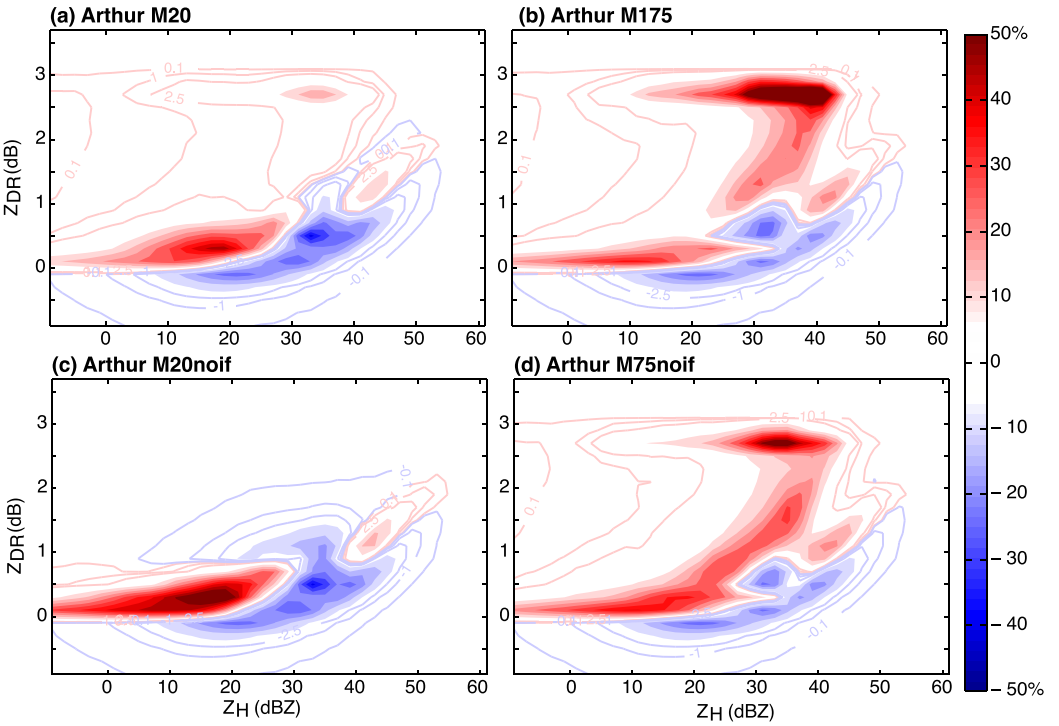

Figure 8. The difference in joint frequency (difference in %) between the simulation and the radar observations as in Figure 2e for Arthur experiments (a) M20, (b) M175, (c) M75noif, and (d) M20noif.

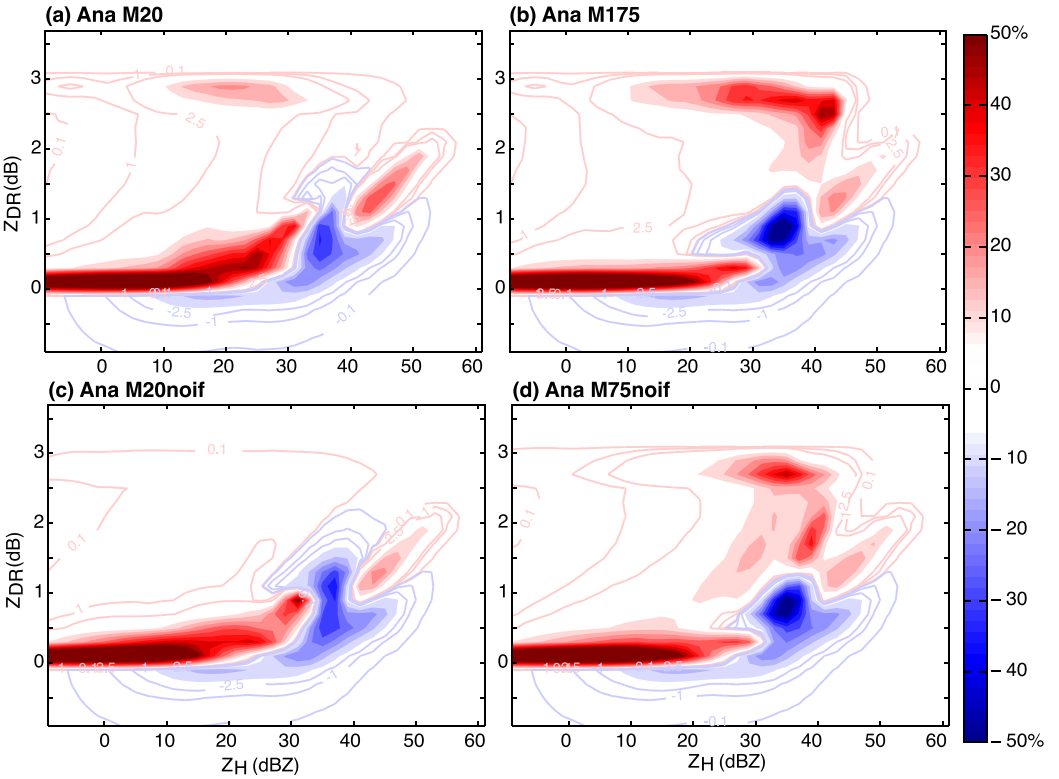

Figure 9. As in Figure 8 but for Ana.

values of negative Z_{DR} that show a negative difference (blue) in Figures 8 and 9 are unphysical noise in the observations. Furthermore, NEXRAD S-band (10 cm) radars do not have sufficient sensitivity to detect very light rain ($Z_H < 10$ dBZ) at longer ranges from the radar when operating in a convective scanning mode. The radar simulator does not include effects of attenuation or beam broadening, and has a perfect sensitivity. It is likely that regions of disagreement at low Z_H are not errors of the Thompson-Eidhammer parameterization but the result of comparing the output of a "perfect" simulator to an imperfect radar. Microphysical considerations and disdrometer measurements suggest that Z_{DR} should approach zero as Z_H approaches zero and raindrops become spherical [e.g., *Kumjian*, 2013, Figure 2], but the low frequency of these drops in the radar observations is likely due to undersampling.

Though the modifications of M20noif have a profound effect on the radar variables in the TC simulations, none of the experiments result in a notable degradation of the maximum 10 m wind speed forecast. The root-mean-square of the maximum 10 m wind speed error for experiments M20, M75noif, and M20noif are within 0.5 m s^{-1} of the RMS error of Arthur in the control simulation, and within 1 m s^{-1} for Ana. The RMS wind speed error for the M175 simulations is within 2 m s^{-1} of the control for both storms. We note that these comparison values are based on a modification of the RMS error of the maximum 10 m wind speed for Ana M75 from the value presented in BBF16 to 9.9 m s^{-1} due to the release of an updated best track record. Though modifications to the microphysical parameterization clearly have nonlinear effects on the precipitation structure (see Figures 5 and 6), it is not surprising that there is little effect on the intensity of the TC for two reasons: First, the modifications do not directly change the mass mixing ratio of rain or snow, and thus have a secondary effect on the diabatic heating rate through changes in the DSD rather than the mass available for condensation or evaporation. Second, the modifications generally have the most effect in stratiform regions of very low rain and snow mixing ratio outside of convective regions, and therefore do not play a large role in changing the precipitation or heating in the eyewall. However, changing the DSD can greatly affect rain evaporation, subsequent downdrafts, and cold pools in the stratiform region [*Eastin et al*., 2012; *Morrison et al*., 2012] and it is reasonable to expect that a longer simulation would show greater differences in the intensity and structure of the simulated TCs.

3.3. Idealized Squall Line Tests

To confirm the generality of the results, additional tests using a different meteorological scenario were conducted. A comprehensive examination of the impacts of raindrop breakup on DSDs in simulations of a midlatitude squall line were reported in *Morrison et al*. [2012]. Tests were conducted here using WRF v3.7.1 with a very similar configuration to *Morrison et al*. [2012] based on the squall line that occurred in central Oklahoma on 20 June 2007. The idealized model configuration consisted of a 1 km horizontal grid spacing using the Thompson-Eidhammer scheme with open lateral boundaries in the across-line (x) direction, and periodic lateral boundary conditions in the along-line (y) direction. The simulation was initialized using artificial low-level convergence by decelerating the zonal wind in the center of the domain for the first hour, producing a more balanced condition for producing the uplift to initiate the squall line than an artificial temperature perturbation. Additional details of the model configuration and the meteorological conditions of this case are described in *Morrison et al*. [2012].

The results of the tests after 6 h of simulation time are shown in Figures 10 and 11. The structure at 6 h was selected for comparison with the observations shown in Figure 12 due to an approximate similarity in the maturity and width of the squall line. The classic leading convective line and trailing stratiform region are well simulated with corresponding changes in the radar reflectivity and median drop size, although the typical weak echo transition zone between the two regions is not evident. Comparisons between the M20noif and M75 parameterizations in Figure 10 indicate a reduction in the reflectivity and median drop size in the stratiform region in the M20noif experiment, similar to that seen in the hurricane simulations. Minimal changes are found in the leading convective line between the two tests, providing further evidence that the primary effect of the parameter change is due to melting of snow in light precipitating regions.

The effect of increased drop breakup on the simulations is shown in Figure 11. The median drop size is reduced through more aggressive breakup and self-collection in both the M20Efrr and M75Efrr experiments, but to a much lesser extent than the effect of changes in the melting parameter. Changes in the stratiform region of the M20Efrr experiment are almost negligible compared to M20noif, while more substantial drop size reductions are evident in the convective region. In the M75Efrr case, drop size reductions are evident

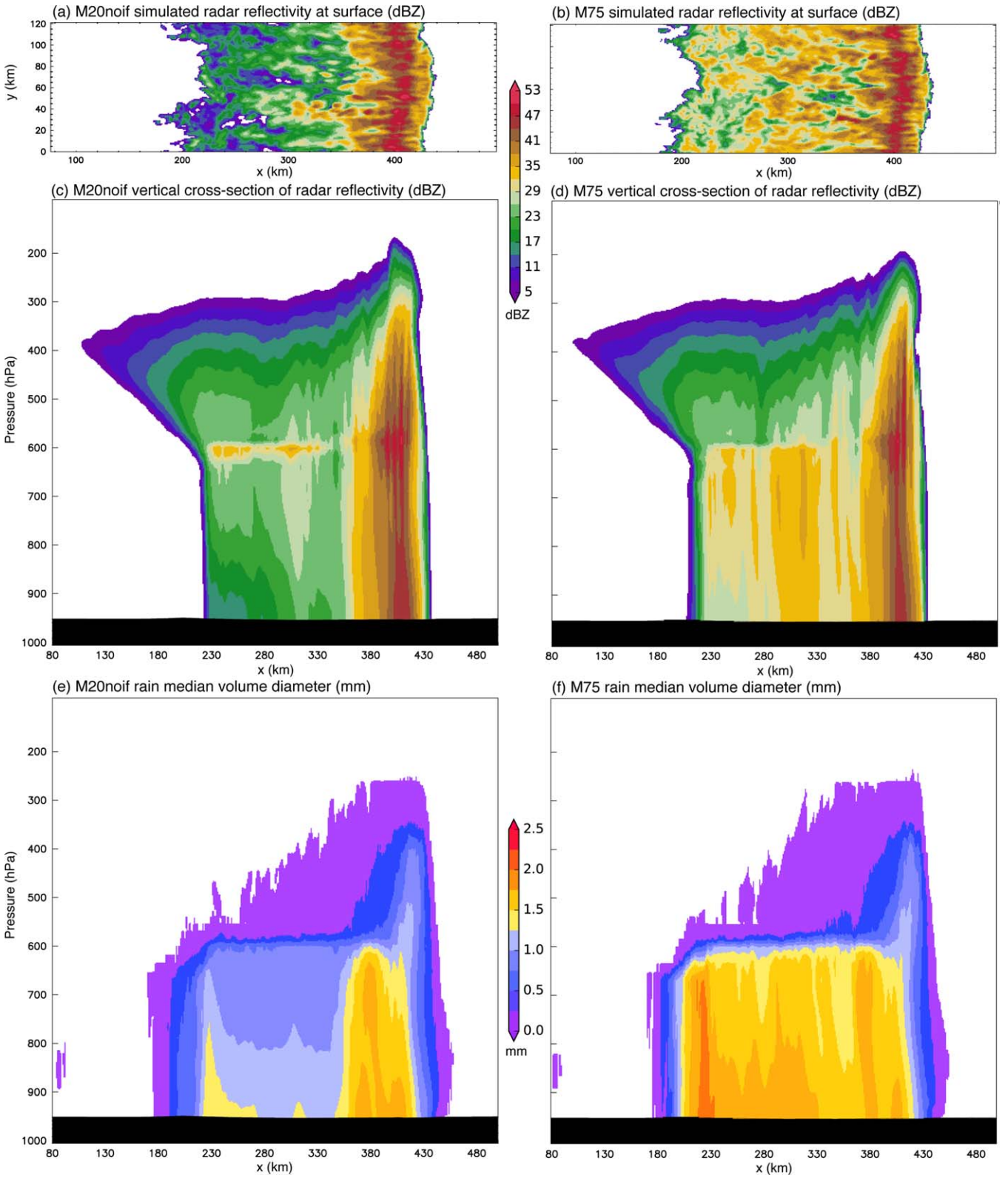

Figure 10. Idealized squall line experiments using (left column) M20noif and (right column) M75. Top row (a, b) shows surface radar reflectivity in dBZ, middle row (c, d) shows vertical cross section of line-averaged radar reflectivity, and bottom row (e, f) shows vertical cross section of line-averaged median drop diameter in mm.

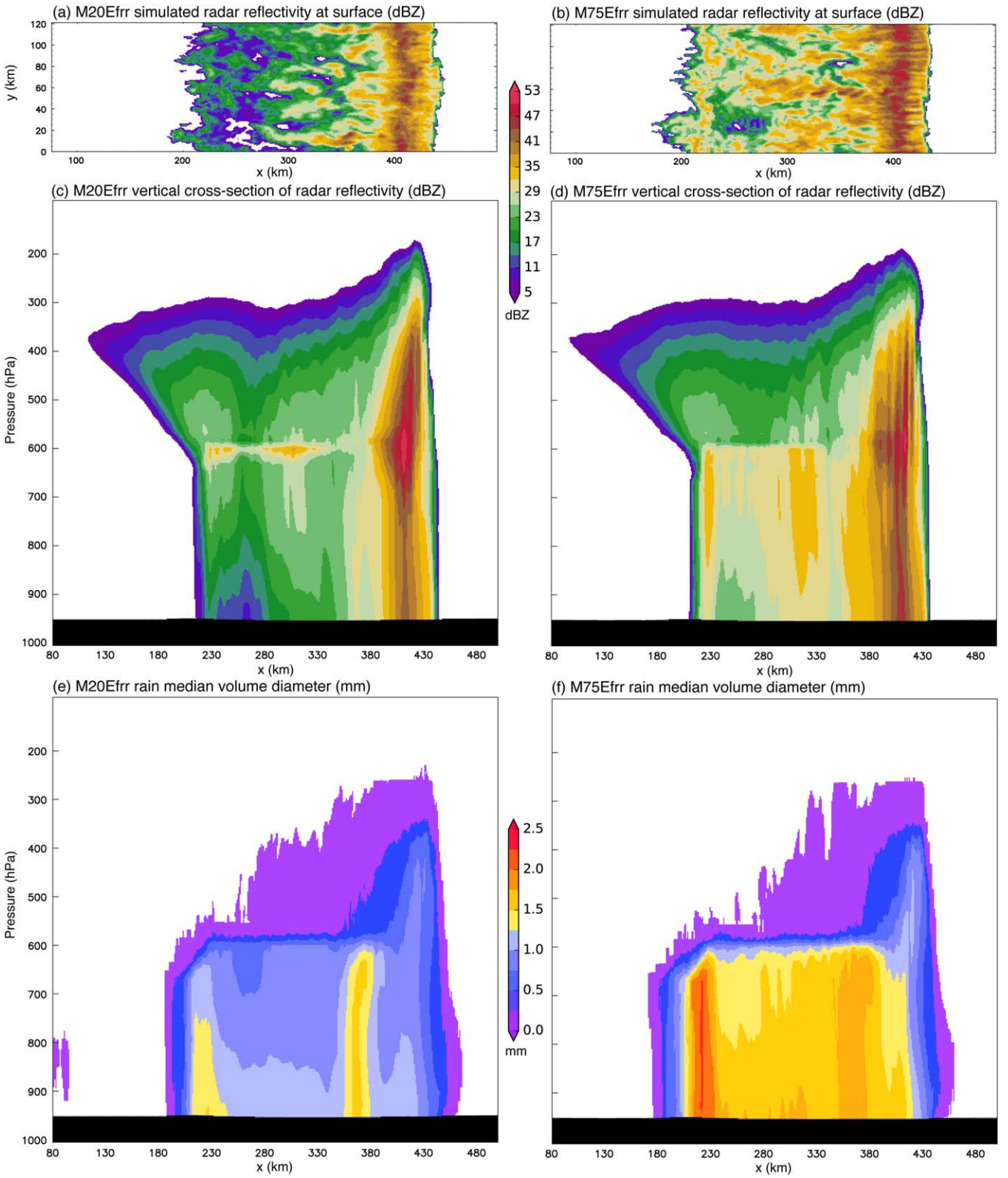

Figure 11. As in Figure 10 but using (left column) M20Efrr and (right column) M75Efrr. See Table 1 for experimental details.

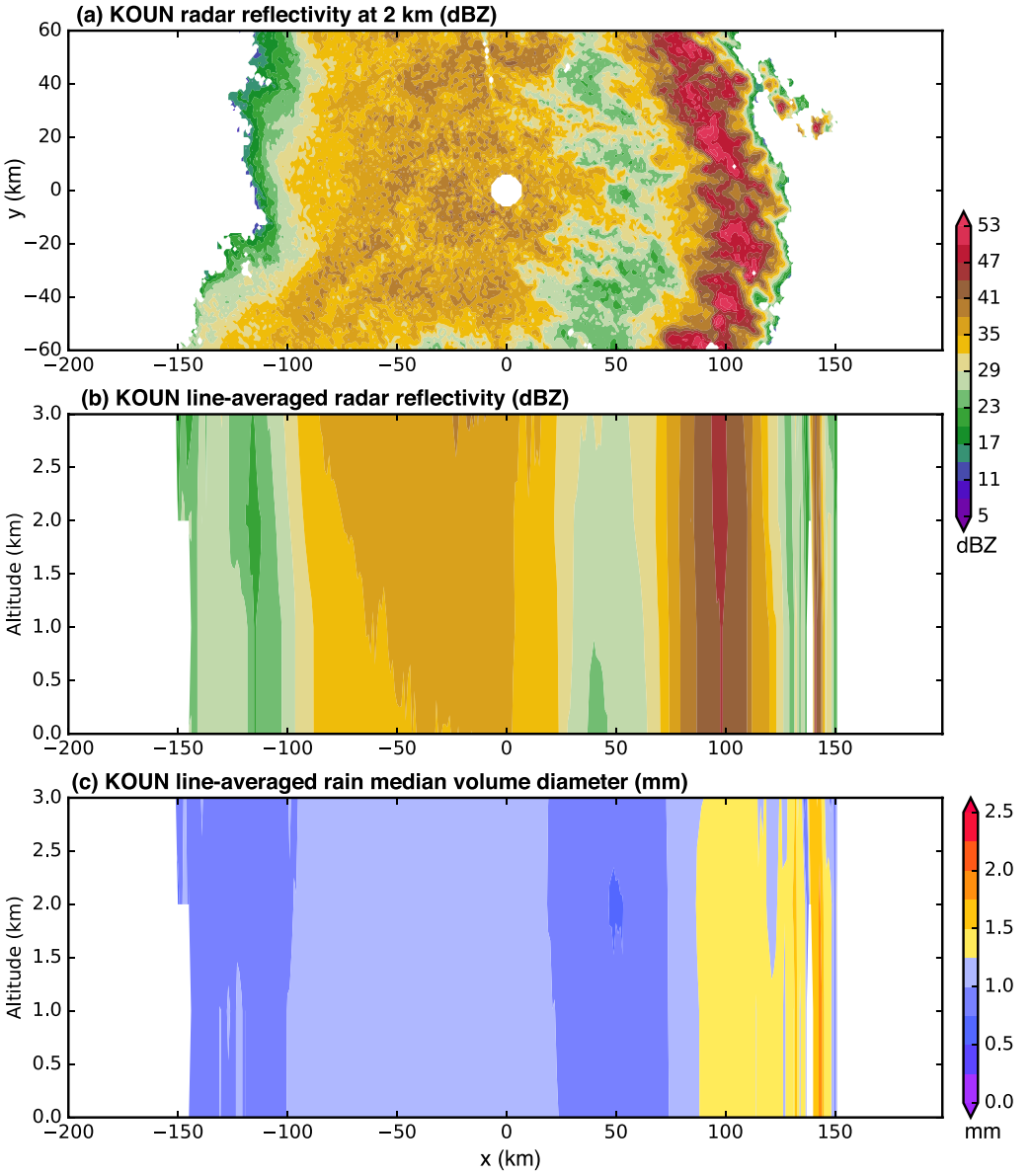

Figure 12. As in Figure 11 but for polarimetric radar data from KOUN radar at 0800 UTC 20 June 2007. Radar data have been rotated 45° in azimuth for easier comparison with the simulation. Top plot (a) shows radar reflectivity at 2 km in dBZ, middle plot (b) shows vertical cross section of line-averaged radar reflectivity below 3 km, and bottom plot (c) shows line-averaged median drop diameter in mm below 3 km.

throughout most of the squall line, but the median volume diameter actually increases slightly at the trailing end of the line. These results confirm that changes in the drop breakup parameterization are primarily effective in regions with large drops above the specified median diameter threshold, and have limited effects in regions with small drops. In other words, the drop breakup process is not very relevant unless the drops are large enough for breakup to actually occur.

Validation of the simulation using polarimetric radar data from the KOUN radar is shown in Figure 12. Comparison of the radar data is limited to below 3 km altitude as in the hurricane cases to focus on liquid raindrops, and the Z_{DR} is converted to median drop size as shown in Figure 3. The line-averaged radar reflectivity and median drop size at 0800 UTC generally compare better with the M20noif simulation than the other tests, although the simulated reflectivity is weaker than the observations. Median drop sizes in the trailing stratiform are consistently near 1.0 mm, which is in good agreement with simulations using the reduced melting parameter. The more aggressive drop breakup in M20Efrr reduces the reflectivity and

median drop size too much in the leading convective line compared to the radar observations. While the M75 and M75Efrr tests compare favorably in the leading convective line, they compare poorly in the stratiform region with a median drop size that is too large. The M20noif test produces the best results compared with the radar observations in both the convective and stratiform regions similar to the hurricane cases. These tests provide further evidence that the parameterization of melting snow is the primary contributor to the discrepancies between the simulations and radar observations described above, and suggest that the results are more generally applicable than to just hurricanes.

4. Conclusions

This study expanded upon the results of BBF16 by modifying the aerosol-aware Thompson-Eidhammer bulk microphysical scheme that was found to be one of the most accurate for TC simulations using a high-resolution WRF experimental framework. It has been shown here that the interface between the single-moment representation of snow and the double-moment representation of rain was a significant source of discrepancies between radar observations of hurricanes Arthur and Ana (both 2014) and simulated radar observations from WRF. In particular, the number production of rain from snow melting contained a tunable parameter originally intended to reduce unreasonably large numbers of tiny particles, but the parameter was found to be too aggressive. An additional conditional statement in the original scheme suppressed any rain number production from snow melting when the snow mixing ratio was below a low threshold, but this was also found to contribute to rain drop size distributions that had a larger median drop size than radar observations. The simulations found to produce a result that was most consistent with the radar observations involved two modifications of the Thompson-Eidhammer parameterization to (a) increase the number production of rain drops from snow melting by increasing the term that artificially reduced the number of particles melting and (b) remove the conditional statement to allow number production of rain drops from snow melting at any snow mixing ratio and irrespective of temperature. Additional tests with an idealized midlatitude squall line confirm the results from the hurricane simulations, and further demonstrate that modifications to the self-collection efficiency produced a slight degradation in the simulated drop sizes in deep convective regions.

We note that these results are consistent for two hurricanes in different ocean basins and an idealized continental squall line with variable environmental conditions, but acknowledge that further testing in different meteorological conditions needs to be conducted for further validation. Some features such as cold pools can be particularly sensitive to the DSD in light stratiform precipitation, and nonlinear effects resulting from these modifications over longer simulations may play a role in the mesoscale organization of midlatitude and tropical convection. In part due to the results from this study, modifications have been made to the aerosol-aware Thompson-Eidhammer microphysical scheme in WRF V3.8.1, changing m from -0.75 to -0.25 and allowing rain number production from snow melting at any snow mixing ratio amount. Similar modifications to the rain number production from graupel melting processes are also incorporated into the Thompson-Eidhammer scheme in WRF V3.8.1 but those modifications are not directly based on the work presented here. The parameter modifications presented here had minimal impact on the wind structure and intensity of the simulated TCs on the short timescales presented here, but further evaluation to refine physical parameters used in Thompson-Eidhammer and other microphysics schemes is recommended. A transition toward fully double-moment microphysics would avoid the conversion from single-moment snow to double-moment rain, but would involve extra computational costs and ultimately would still require accurate parameterization of the physics of ice melting processes. The physics in the mixed-phase region are inherently complex, and as simulations move to fully double-moment or even higher order representations due to increased computational power the microphysical parameterizations must continue to be carefully scrutinized and validated with observations.

Acknowledgments

This study was supported by the Office of Naval Research award N000141512601 and National Science Foundation CAREER award AGS-1349881. Computing resources from NCAR's Computational and Information Systems Laboratory (CISL) Yellowstone HPC facility were used for selected WRF simulations [*Computational and Information Systems Laboratory*, 2012], and GFS analyses were obtained from CISL's Research Data Archive [*National Centers for Environmental Prediction*, 2000]. Best track data were obtained from the HURDAT2 data set produced by the NOAA's National Hurricane Center [*Landsea et al.*, 2015]. Level II radar data from the KLTX, KMHX, PHKI, and PHMO radars were obtained from the NOAA National Climatic Data Center, and we are grateful to Sarah Tessendorf for providing the KOUN radar data. The authors would like to thank Andrew Frambach and Jonathan Martinez for their assistance in processing the Level II radar data. G. Thompson gratefully acknowledges the support of the Developmental Testbed Center. The authors are grateful for the thoughtful feedback of two anonymous reviewers. All the data and input files used in this study are available from the authors upon request (mmbell@colostate.edu).

References

Berg, R. (2015), Hurricane Arthur (AL012014), *Tropical Cyclone Report*, Natl. Hurricane Cent., Miami, Fla. [Available at http://www.nhc.noaa.gov/data/tcr/AL012014_Arthur.pdf.]

Brandes, E. A., G. Zhang, and J. Vivekanandan (2004a), Drop size distribution retrieval with polarimetric radar: Model and application, *J. Appl. Meteorol.*, *43*(3), 461–475.

Brandes, E. A., G. Zhang, and J. Vivekanandan (2004b), Comparison of polarimetric radar drop size distribution retrieval algorithms, *J. Atmos. Oceanic Technol.*, *21*, 584–598.

Brown, B. R., M. M. Bell, and A. J. Frambach (2016), Validation of simulated hurricane drop size distributions using polarimetric radar, *Geophys. Res. Lett.*, *43*, 910–917, doi:10.1002/2015GL067278.

Computational and Information Systems Laboratory (2012), Yellowstone: IBM iDataPlex system (University Community Computing), Natl. Cent. for Atmos. Res., Boulder, Colo. [Available at http://n2t.net/ark:/85065/d7wd3xhc.]
Cunningham, J. G., W. D. Zittel, R. R. Lee, and R. L. Ice (2013), Methods for identifying systematic differential reflectivity (ZDR) biases on the operational WSR88D network, in *36th Conference on Radar Meteorology*, Amer. Meteor. Soc., Breckenridge, Colo.
Davis, C., W. Wang, J. Dudhia, and R. Torn (2010), Does increased horizontal resolution improve hurricane wind forecasts?, *Weather Forecast.*, *25*(6), 1826–1841.
DeHart, J. C., R. A. Houze, and R. F. Rogers (2014), Quadrant distribution of tropical cyclone inner-core kinematics in relation to environmental shear, *J. Atmos. Sci.*, *71*, 2713–2732.
DeMaria, M., C. R. Sampson, J. A. Knaff, and K. D. Musgrave (2014), Is tropical cyclone intensity guidance improving?, *Bull. Am. Meteorol. Soc.*, *95*(3), 387–398, doi:10.1175/BAMS-D-12-00240.1.
Doyle, J. D., S. Hodur, S. Chen, Y. Jin, J. R. Moskaitis, S. Wang, E. A. Hendricks, H. Jin, and T. A. Smith (2014), Tropical cyclone prediction using COAMPS-TC, *Oceanography*, *27*(3), 104–115.
Dudhia, J. (1989), Numerical study of convection observed during winter monsoon experiment using a mesoscale two-dimensional model, *J. Atmos. Sci.*, *46*(20), 3077–3107.
Eastin, M., T. Gardner, M. Link, and K. Smith (2012), Surface cold pools in the outer rainbands of Tropical Storm Hanna (2008) near landfall, *Mon. Weather Rev.*, *140*(2), 471–491, doi:10.1175/MWR-D-11-00099.1.
Ek, M. B. (2003), Implementation of Noah land surface model advances in the National Centers for Environmental Prediction operational mesoscale Eta model, *J. Geophys. Res.*, *108*(D22), 8851, doi:10.1029/2002JD003296.
Emanuel, K., and F. Zhang (2016), On the predictability and error sources of tropical cyclone intensity forecasts, *J. Atmos. Sci.*, *73*, 3739–3747.
Fovell, R. G., K. L. Corbosiero, and H.-C. Kuo (2009), Cloud microphysics impact on hurricane track as revealed in idealized experiments, *J. Atmos. Sci.*, *66*(6), 1764–1778.
Fovell, R. G., Y. P. Bu, K. L. Corborsiero, W.-W. Tung, Y. Cao, H.-C. Kuo, L.-H. Hsu, and H. Su (2016), Influence of cloud microphysics and radiation on tropical cyclone structure and motion, in Multiscale Convection-Coupled Systems in the Tropics: A Tribute to Dr. Michio Yanai, *Meteor. Monogr.*, *56*, 11.1–11.27.
Hence, D. A., and R. A. Houze (2011), Vertical structure of hurricane eyewalls as seen by the TRMM precipitation radar, *J. Atmos. Sci.*, *68*(8), 1637–1652.
Hong, S.-Y., Y. Noh, and J. Dudhia (2006), A new vertical diffusion package with an explicit treatment of entrainment processes, *Mon. Weather Rev.*, *134*, 2318–2341.
Igel, A. L., M. R. Igel, and S. C. van den Heever (2015), Make it a double? Sobering results from simulations using single-moment microphysics schemes, *J. Atmos. Sci.*, *72*, 910–925.
Jin, Y., et al. (2014), The impact of ice phase cloud parameterizations on tropical cyclone prediction, *Mon. Weather Rev.*, *142*, 606–625.
Jung, Y., M. Xue, and G. Zhang (2010), Simulations of polarimetric radar signatures of a supercell storm using a two-moment bulk microphysics scheme, *J. Appl. Meteorol. Climatol.*, *49*, 146–163.
Kain, J. S., and J. M. Fritsch (1990), A one-dimensional entraining detraining plume model and its application in convective parameterization, *J. Atmos. Sci.*, *47*, 2784–2802.
Khain, A., B. Lynn, and J. Shpund (2015), High resolution WRF simulations of hurricane Irene: Sensitivity to aerosols and choice of microphysical schemes, *Atmos. Res.*, *167*, 129–145.
Kosiba, K., J. Wurman, F. J. Masters, and P. Robinson (2013), Mapping of near-surface winds in Hurricane Rita using finescale radar, anemometer, and land-use data, *Mon. Weather Rev.*, *141*(12), 4337–4349, doi:10.1175/MWR-D-12-00350.1.
Kosiba, K. A., and J. Wurman (2014), Finescale dual-Doppler analysis of hurricane boundary layer structures in Hurricane Frances (2004) at landfall, *Mon. Weather Rev.*, *142*(5), 1874–1891, doi:10.1175/MWR-D-13-00178.1.
Kumjian, M. R. (2013), Principles and applications of dual-polarization weather radar. Part I: Description of the polarimetric radar variables, *J. Oper. Meteorol.*, *1*(19), 226–242.
Landsea, C. W., J. L. Franklin, and J. L. Beven (2015), The revised Atlantic hurricane database (HURDAT2), U.S. Natl. Oceanic and Atmos. Admin. Natl. Weather Serv., Miami, Fla. [Available at http://www.nhc.noaa.gov/data/hurdat/hurdat2-format-atlantic.pdf.]
May, P. T., J. D. Kepert, and T. D. Keenan (2008), Polarimetric radar observations of the persistently asymmetric structure of tropical cyclone ingrid, *Mon. Weather Rev.*, *136*(2), 616–630, doi:10.1175/2007MWR2077.1.
Mlawer, E. J., S. J. Taubman, P. D. Brown, M. J. Iacono, and S. A. Clough (1997), Radiative transfer for inhomogeneous atmospheres: RRTM, a validated correlated-k model for the longwave, *J. Geophys. Res.*, *102*, 16,663–16,682.
Morrison, H., S. A. Tessendorf, K. Ikeda, and G. Thompson (2012), Sensitivity of a simulated midlatitude squall line to parameterization of raindrop breakup, *Mon. Weather Rev.*, *140*(8), 2437–2460, doi:10.1175/MWR-D-11-00283.1.
National Centers for Environmental Prediction, National Weather Service, NOAA, and U.S. Department of Commerce (2000), NCEP FNL operational model global tropospheric analyses, continuing from July 1999 Res. Data Arch. at the Natl. Cent. for Atmos. Res., Comput. and Inf. Syst. Lab., Boulder, Colo. [Available at https://doi.org/10.5065/D6M043C6.]
Nissan, H., and R. Toumi (2013), Dynamic simulation of rainfall kinetic energy flux in a cloud resolving model, *Geophys. Res. Lett.*, *40*, 3331–3336, doi:10.1002/grl.50622.
Pattnaik, S., C. Inglish, and T. N. Krishnamurti (2011), Influence of rain-rate initialization, cloud microphysics, and cloud torques on hurricane intensity, *Mon. Weather Rev.*, *139*, 627–649.
Penny, A. B., P. A. Harr, and J. D. Doyle (2016), Sensitivity to the representation of microphysical processes in numerical simulations during tropical storm formation, *Mon. Weather Rev.*, *144*(10), 3611–3630, doi:10.1175/MWR-D-15-0259.1.
Powell, J. (2014), Hurricane Ana (CP022014), Tropical Cyclone Report, Cent. Pac. Hurricane Cent., Natl. Weather Serv., Honolulu, Hawaii. [Available at http://www.prh.noaa.gov/cphc/summaries/2014/Final-CP022014_Ana_Final.docx.]
Thompson, G., and T. Eidhammer (2014), A study of aerosol impacts on clouds and precipitation development in a large winter cyclone, *J. Atmos. Sci.*, *71*(10), 3636–3658.
Thompson, G., P. R. Field, R. M. Rasmussen, and W. D. Hall (2008), Explicit forecasts of winter precipitation using an improved bulk microphysics scheme. Part II: Implementation of a new snow parameterization, *Mon. Weather Rev.*, *136*, 5095–5115.
Ulbrich, C. W. (1983), Natural variations in the analytical form of the raindrop size distribution, *J. Clim. Appl. Meteorol.*, *22*, 1764–1775.
Wang, M., K. Zhao, M. Xue, G. Zhang, S. Liu, L. Wen, and G. Chen (2016), Precipitation microphysics characteristics of a Typhoon Matmo (2014) rainband after landfall over eastern China based on polarimetric radar observations, *J. Geophys. Res. Atmos.*, *121*, 12,415–12,433, doi:10.1002/2016JD025307.
White, A. B., J. R. Jordan, B. E. Martner, F. M. Ralph, and B. W. Bartram (2000), Extending the dynamic range of an S-band radar for cloud and precipitation studies, *J. Atmos. Oceanic Technol.*, *17*, 1226–1234, doi:10.1175/1520-0426(2000)017<1226:ETDROA>2.0.CO;2.